THE UNIVERSITY of EDINBURGH

Edinburgh Research Explorer

Characterization and modelling of inter-core coupling in coherent fiber bundles

OPEN ACCESS

Characterization and modelling of inter-core coupling in coherent fiber bundles

Antonios Perperidis,[1,2,*] Helen E. Parker,[2] Ahmed Karam-Eldaly,[1] Yoann Altmann,[1] Kevin Dhaliwal,[2] Robert R. Thomson,[3] Michael G. Tanner,[2,3] and Stephen McLaughlin[1]

[1]*Institute of Sensors, Signals and Systems (ISSS), Heriot Watt University, EH14 4AS, UK*
[2]*EPSRC IRC "Hub" in Optical Molecular Sensing & Imaging, MRC Centre for Inflammation Research, Queen's Medical Research Institute (QMRI), University of Edinburgh, EH16 4TJ, UK*
[3]*Institute of Photonics and Quantum Sciences (IPAQS), Heriot Watt University, EH14 4AS, UK*
*A.Perperidis@hw.ac.uk

Abstract: Recent developments in optical endomicroscopy (OEM) and associated fluorescent SmartProbes present a need for sensitive imaging with high detection performance. Inter-core coupling within coherent fiber bundles is a well recognized limitation, affecting the technology's imaging capabilities. Fiber cross coupling has been studied both experimentally and within a theoretical framework (coupled mode theory), providing (i) insights on the factors affecting cross talk, and (ii) recommendations for optimal fiber bundle design. However, due to physical limitations, such as the tradeoff between cross coupling and core density, cross coupling can be suppressed yet not eliminated through optimal fiber design. This study introduces a novel approach for measuring, analyzing and quantifying cross coupling within coherent fiber bundles, in a format that can be integrated into a linear model, which in turn can enable computational compensation of the associated blurring introduced to OEM images.

References and links

1. P. Sharma, A. R. Meining, E. Coron, C. J. Lightdale, H. C. Wolfsen, A. Bansal, M. Bajbouj, J.-P. Galmiche, J. A. Abrams, A. Rastogi, N. Gupta, J. E. Michalek, G. Y. Lauwers, and M. B. Wallace, "Real-time increased detection of neoplastic tissue in Barrett's esophagus with probe-based confocal laser endomicroscopy: final results of an international multicenter, prospective, randomized, controlled trial," Gastrointest. Endosc. **74**(3), 465–472 (2011).
2. M. B. Wallace and P. Fockens, "Probe-based confocal laser endomicroscopy," Gastroenterology **136**(5), 1509–1513 (2009).
3. Y. Pan, J.-P. Volkmer, K. E. Mach, R. V. Rouse, J.-J. Liu, D. Sahoo, T. C. Chang, T. J. Metzner, L. Kang, M. van de Rijn, E. C. Skinner, S. S. Gambhir, I. L. Weissman, and J. C. Liao, "Endoscopic molecular imaging of human bladder cancer using a CD47 antibody," Sci. Translational Med. **6**(260), 260ra148 (2014).
4. L. Thiberville, S. Moreno-Swirc, T. Vercauteren, E. Peltier, C. Cavé, and G. Bourg Heckly, "In Vivo Imaging Of The Bronchial Wall Microstructure Using Fibered Confocal Fluorescence Microscopy," Am. J. Respir. Crit. Care Med. **175**(1), 22–31 (2007).
5. T. Aslam, A. Miele, S. V. Chankeshwara, A. Megia-Fernandez, C. Michels, A. R. Akram, N. McDonald, N. Hirani, C. Haslett, M. Bradley, and K. Dhaliwal, "Optical molecular imaging of lysyl oxidase activity - detection of active fibrogenesis in human lung tissue," Chem. Sci. (Camb.) **6**(8), 4946–4953 (2015).
6. F. S. Fuchs, S. Zirlik, K. Hildner, J. Schubert, M. Vieth, and M. F. Neurath, "Confocal laser endomicroscopy for diagnosing lung cancer in vivo," Eur. Respir. J. **41**(6), 1401–1408 (2013).
7. L. Thiberville, M. Salaün, S. Lachkar, S. Dominique, S. Moreno-Swirc, C. Vever-Bizet, and G. Bourg-Heckly, "In vivo confocal fluorescence endomicroscopy of lung cancer," J. Thorac. Oncol. **4**(9), S48–S51 (2009).
8. L. Thiberville, M. Salaün, S. Lachkar, S. Dominique, S. Moreno-Swirc, C. Vever-Bizet, and G. Bourg-Heckly, "Human in vivo fluorescence microimaging of the alveolar ducts and sacs during bronchoscopy," Eur. Respir. J. **33**(5), 974–985 (2009).

9. L. Thiberville, M. Salaün, S. Lachkar, S. Dominique, S. Moreno-Swirc, C. Vever-Bizet, and G. Bourg-Heckly, "Confocal fluorescence endomicroscopy of the human airways," in Proceedings of the American Thoracic Society (American Thoracic Society, 2009), pp. 444–449.

10. R. C. Newton, S. V. Kemp, G.-Z. Yang, D. S. Elson, A. Darzi, and P. L. Shah, "Imaging parenchymal lung diseases with confocal endomicroscopy," Respir. Med. **106**(1), 127–137 (2012).

11. M. Pierce, D. Yu, and R. Richards-Kortum, "High-resolution Fiber-optic Microendoscopy for in situ Cellular Imaging," J. Vis. Experiments **47**, 2306 (2011).

12. N. Krstajić, A. R. Akram, T. R. Choudhary, N. McDonald, M. G. Tanner, E. Pedretti, P. A. Dalgarno, E. Scholefield, J. M. Girkin, A. Moore, M. Bradley, and K. Dhaliwal, "Two-color widefield fluorescence microendoscopy enables multiplexed molecular imaging in the alveolar space of human lung tissue," J. Biomed. Opt. **21**(4), 46009 (2016).

13. N. Avlonitis, M. Debunne, T. Aslam, N. McDonald, C. Haslett, K. Dhaliwal, and M. Bradley, "Highly specific, multi-branched fluorescent reporters for analysis of human neutrophil elastase," Org. Biomol. Chem. **11**(26), 4414–4418 (2013).

14. A. R. Akram, N. Avlonitis, A. Lilienkampf, A. M. Perez-Lopez, N. McDonald, S. V. Chankeshwara, E. Scholefield, C. Haslett, M. Bradley, and K. Dhaliwal, "A labelled-ubiquicidin antimicrobial peptide for immediate in situ optical detection of live bacteria in human alveolar lung tissue," Chem. Sci. (Camb.) **6**(12), 6971–6979 (2015).

15. A. W. Snyder and P. McIntyre, "Crosstalk between light pipes," J. Opt. Soc. Am. **66**(9), 877–882 (1976).

16. A. W. Snyder, "Coupled-mode theory for optical fibers," J. Opt. Soc. Am. **62**(11), 1267–1277 (1972).

17. K. L. Reichenbach and C. Xu, "Numerical analysis of light propagation in image fibers or coherent fiber bundles," Opt. Express **15**(5), 2151–2165 (2007).

18. J. Wang and S. K. Nadkarni, "The influence of optical fiber bundle parameters on the transmission of laser speckle patterns," Opt. Express **22**(8), 8908–8918 (2014).

19. N. Ortega-Quijano, J. L. Arce-Diego, and F. Fanjul-Vélez, "Quality limiting factors of imaging endoscopes based on optical fiber bundles," in Proc. SPIE 6991 (SPIE, 2008), pp. 69910U.

20. N. Ortega-Quijano, F. Fanjul-Vélez, and J. L. Arce-Diego, "Optical crosstalk influence in fiber imaging endoscopes design," Opt. Commun. **283**(4), 633–638 (2010).

21. N. Ortega-Quijano, F. Fanjul-Vélez, I. Salas-García, Ó. R. Hernández-Cubero, and J. L. Arce-Diego, "Analysis of optical crosstalk in flexible imaging endoscopes based on multicore fibers," in Proc. SPIE 7715 (SPIE, 2010), pp. 77152B.

22. X. Chen, K. L. Reichenbach, and C. Xu, "Experimental and theoretical analysis of core-to-core coupling on fiber bundle imaging," Opt. Express **16**(26), 21598–21607 (2008).

23. H. Wood, K. Harrington, J. M. Stone, T. A. Birks, and J. C. Knight, "Quantitative characterization of endoscopic imaging fibers," Opt. Express **25**(3), 1985–1992 (2017).

24. J. L. Starck, E. Pantin, and F. Murtagh, "Deconvolution in Astronomy: A Review," Publ. Astron. Soc. Pac. **114**(800), 1051–1069 (2002).

25. M. R. Banham and A. K. Katsaggelos, "Digital image restoration," IEEE Signal Process. Mag. **14**(2), 24–41 (1997).

26. J. M. Bioucas-Dias, M. A. T. Figueiredo, and J. P. Oliveira, "Total Variation-Based Image Deconvolution: a Majorization-Minimization Approach," in *Proceedings of IEEE International Conference on Acoustics Speech and Signal Processing* (IEEE, 2006), pp. 861–864.

27. A. Wong, X. Y. Wang, and M. Gorbet, "Bayesian-based deconvolution fluorescence microscopy using dynamically updated nonstationary expectation estimates," Sci. Rep. **5**, 10849 (2015).

28. J. M. Stone, H. A. Wood, K. Harrington, and T. A. Birks, "Low index contrast imaging fibers," Opt. Lett. **42**(8), 1484–1487 (2017).

29. S. Suzaki and K. Seto, "Standard specifications for image fibers" (Fujikura Ltd., 2016), retrieved 2017, http://www.fujikura.co.jp/eng/products/optical/appliedoptics/03/2050110_12902.html.

30. T. Vercauteren, "Image Registration and Mosaicing for Dynamic In Vivo Fibered Confocal Microscopy," (Mines ParisTech, Paris, 2008).

31. C. Studholme, D. L. G. Hill, and D. J. Hawkes, "An overlap invariant entropy measure of 3D medical image alignment," Pattern Recognit. **32**(1), 71–86 (1999).

32. A. Karam Eldaly, Y. Altmann, A. Perperidis, N. Krstajić, T. R. Choudhary, K. Dhaliwal, and S. McLaughlin, "Deconvolution and Restoration of Optical Endomicroscopy Images" (2017), retrieved 2017, https://arxiv.org/abs/1701.08107.

33. F. Sroubek and J. Flusser, "Multichannel blind iterative image restoration," IEEE Trans. Image Process. **12**(9), 1094–1106 (2003).

1. Introduction

Optical endomicroscopy (OEM) is an emerging, fibre-based medical imaging tool with clinical and pre-clinical utility. The technology employs a proximal light source, laser scanning or Light Emitting Diode (LED) illumination, linked to a flexible multicore fibre, performing microscopic fluorescent imaging at its distal end. The diameter of the packaged

fibre can be as small as a 500μm, enabling the real-time imaging of tissues that were previously inaccessible through conventional endoscopy. OEM has been deployed to image a range of organ systems, including the gastro-intestinal [1, 2], urological [3] and the respiratory tracts. In pulmonary OEM, auto-fluorescence (at 488nm) generated through the abundant elastin and collagen has enabled the exploration of the distal pulmonary tract [4] as well as the assessment of the respiratory bronchioles and alveolar gas exchanging units of the distal lung [5]. OEM has been used clinically in the lung for the detection of lung cancer [6, 7] and has been used to assess the distal lung [8, 9] including the imaging of parenchymal lung diseases [10].

Fibered Confocal Fluorescent Microscopy (FCFM), also referred to as probe-based confocal laser endomicroscopy (pCLE), is currently the most widely used clinical OEM platform. However, there have recently been a number of studies describing novel, flexible and versatile OEM architectures [11], employing LED illumination sources, capable of imaging at multiple acquisition wavelengths [12]. Furthermore, there has been an effort to develop molecularly targeted fluorescent SmartProbes that can bind and amplify fluorescence in the presence of inflammation [13], bacteria [14] and fibrogenesis [5], necessitating for sensitive imaging platforms. This emerging requirement for low limits of detection becomes of paramount importance when imaging small targets such as bacteria superimposed upon highly autofluorescent structures like elastin strands in the distal lung [12].

Inter-core coupling is a well recognised limitation in coherent fibre bundles, resulting in blurring of the imaged structures and consequently a worsening in the associated limits of detection. Due to the nature of data acquisition, confocal imaging offers a number of distinct advantages to widefield imaging, including the ability to control depth of focus (optical sectioning), suppressing the background information outside the focal plane. Furthermore, in confocal endomicroscopy, the detector pinhole aperture can mask out light coupled to neighbouring cores before reaching the detector. Consequently, the effect of inter-core coupling in imaging capabilities is inherently of greater importance in widefield endomicroscopy.

Coupled mode theory [15, 16] provides a theoretical framework to model the effect of cross-talk between neighbouring fibre cores. A number of studies [17–21] have employed coupled mode theory to study the effect of a range of features on inter-core coupling, such as the fibre length, optogeometrical parameters (core size, cladding size, core distance), wavelength and core size variability. Other studies have adopted an experimental approach to assessing the effect of inter-core coupling. Chen et al. [22] illuminated individual cores in coherent fibre bundles at different wavelengths and quantified the light spread to neighbouring cores, comparing the experimental findings with associated numerical simulations. A recent study [23] describes a novel approach for quantitatively assessing the effect of inter-core coupling on coherent fibre bundles by the projection of an interference pattern and analysis of the Fourier transform of the acquired images deriving a measure of fidelity of the pattern referred to as Fourier contrast. The aforementioned studies have provided insights on the factors affecting fibre cross talk, and its effect on imaging fibre-bundles, providing solutions and recommendations for the optimal design, selection and optimisation of fibre bundles for certain applications. However, due to physical limitations, such as the trade-off between cross coupling and core-density (resolution), cross coupling can be suppressed yet not eliminated through optimal fibre design.

Imaging systems are characterised by their ability to resolve fine detail in the imaged scene. Image resolution quantifies this ability as the minimum distance between two infinitely small point light sources that can be discretely imaged. For a variety of reasons, typically associated with each specific imaging modality, blur in the form of non-random spread is introduced to the recorded signal. A point spread function (PSF) describes the response (blur) of an imaging system to a point source. Consequently, the recorded image v (vectorised) can be modelled as

$$v = Hu + w \qquad\qquad (1)$$

where u is the original signal, H is the matrix representation of a convolution operator modelling the spread of light as described by the system's PSF (as well as any other source of image blur present), and w representing additive observation noise. A plethora of studies have attempted to estimate u from v, effectively de-blurring the recorded signal [24, 25]. The algorithms range from simple numerical estimations through inverse filtering, to sophisticated optimisation-based [26] and simulation-based approaches [27]. The aim of this study is to introduce a novel approach for measuring, analysing and quantifying inter-core coupling within coherent fibre bundles, in a format that can then be integrated in a linear model, as in Eq. (1). A robust and repeatable inter-core coupling characterisation and modelling can then enable image deconvolution and reconstruction approaches to computationally compensate for the associated blurring introduced to OEM images. Since, there are already OEM devices imaging at multiple wavelengths, all proposed acquisition and analysis approaches are performed at two wavelengths (520nm and 635nm) as in [12].

The rest of the paper is organized as follows: Section 2 describes the methodology employed in this study, describing the experimental setup, the acquisition protocol and the subsequent data analysis. Section 3 displays the relevant results on the cross coupling quantification, the robustness of acquisition approach, and the effect of cross coupling on simulated data. Finally, the proposed methods and corresponding results are discussed in Section 4.
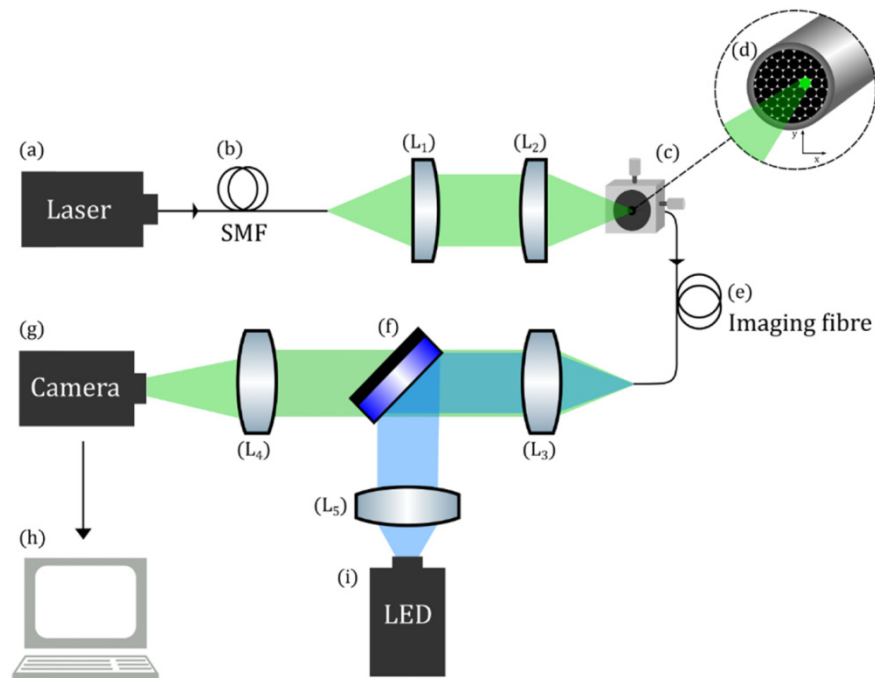

Fig. 1. Optical system utilised for illuminating (laser at 635nm and 520nm) a single core within a coherent fibre bundle, and recording the coupling of light across its immediate and extended neighbouring cores. A 470nm LED light was also employed to acquire widefield microscopy (WFM) images of the fibre cores.

2. Methodology

2.1 Experimental setup

The optical setup assembled and employed for characterising inter-core coupling, as illustrated in Fig. 1, was comprised entirely of off-the-self commercial components. A laser source was coupled into a single mode fibre (SMF) (SM400, Thorlabs, USA). The output light spot of the SMF was resized, through a pair of aspheric lenses (L_1 and L_2) (C340TMD-A and C230TMD-A, Thorlabs, USA), to illuminate individual cores of the coherent fibre (FIGH-30-650S, Fujikura). In this study, inter-core coupling was assessed at both 520nm and 635nm wavelengths (LP520-SF15 and LP635-SF8 respectively, Thorlabs, USA). The characterised fibre bundle was doped silica-based with high numeric aperture (NA~0.4), step-index cores [17, 22, 28]. Table 1 provides detailed information on the multicore fibre's technical characteristics. The front end of the coherent fibre bundle was mounted on an x-y translation stage (ST1XY-D, Thorlabs, USA), while the back end of the imaging fibre was mounted in the imaging plane of a 20x (0.5 NA) infinity-corrected microscope objective (UPLFLN 20X, Olympus, Japan) (L_3). The fibre was positioned and maintained without an intentional curvature (straight) throughout the experiment. After the objective, the light was transmitted through a custom two band dichroic mirror (Cairn Research, USA) and focused through a 250mm focal length tube lens (AC254-250-A, Thorlabs, USA) (L_4) onto a monochromatic CMOS camera (GS3-U3-23S6M-C Grasshopper, Point Grey, Canada) with output to a PC. Additional LED illumination (M470L3, Thorlabs, USA), collimated through an anti-reflection (AR) coated achromatic condenser lens (ACL2520-A, Thorlabs, USA) (L_5) and reflected by a dichroic mirror into the objective L_5, enabled flood illumination and imaging of the coherent fibre bundle onto the CMOS camera.

Table 1. Fujikura coherent fibre bundle specifications [29].

	FIGH-30-650S
Core number (x10^3)	30 ± 3
Field-of-view diameter (μm)	600 ± 30
Fibre diameter (μm)	650 ± 30
Coating diameter (μm)	750 ± 50

2.2 Acquisition protocol

2.2.1 Specifying optical setup

Analysis of the core cross-talk within a coherent fibre bundle relies heavily on a robust method for efficiently coupling light into individual cores, preventing the illumination spot overlapping neighbouring cores. In order to achieve this, the size of the illuminating source as well as the range of core sizes within the coherent fibre bundle were approximated. This information enabled the appropriate resizing of the illumination spot. More precisely, for each acquisition wavelength (520nm and 635nm), the in-focus point spread function (PSF) of the laser source coupled into a single mode fibre (SM400, Thorlabs) was imaged directly onto a monochromatic CMOS camera (by replacing the imaging fibre in the optical setup, Fig. 1). A Gaussian distribution was fit ($r^2 > 0.998$) across the horizontal and vertical profiles of the PSF, with both profiles demonstrating nearly identical spreads ($\sigma_h = \sigma_v = \sigma$). The radius of the laser spot, y_1, was approximated as 4σ accounting for $\sim 96\%$ of the overall light. The coherent fibre bundle was then placed into the same imaging plane and excited by a 470 nm LED generating a red auto-fluorescent response at each individual core. The resulting auto-fluorescent image was used to detect the location of each core and estimate the distance d to its nearest-neighbour. The average nearest-neighbour distance $\bar{d}$ amongst all the cores in widefield image was employed as an indirect estimate of an upper spot size bound to

minimize neighbouring core illumination. Table 2 summarises the core and spot size approximations for the optical setup illustrated in Fig. 2. Aspheric lenses L_1 and L_2, with focal lengths of $f_1 = 4.03mm$ and $f_2 = 4.51mm$, respectively, were pairwise selected to optimally resize (enlarge) the laser spot radius, y_1, minimising the overlapping illumination of neighbouring cores (avoiding a laser illumination spot $> \bar{d}$), while maximising illumination coverage of individual cores, to avoid illuminating individual higher order modes. Light illuminating the cladding region is in theory not expected to couple into the neighbouring cores, which is also verified in practice when moving the laser spot across the cladding between cores. Consequently, illuminating the cladding regions should not adversely affect the subsequent coupling extent measurements. For the optical setup illustrated in Fig. 2, the relation between spot sizes and focal lengths could be described as

$$\frac{y_1}{f_1} = \frac{y_2}{f_2} \tag{2}$$

with y_2 being the resized laser spot radius. L_1 and L_2 were thus selected, amongst a finite set of options, such that,

$$\arg_{f_1, f_1} \min \left| \bar{d} - \left(\frac{f_2}{f_1} \right) 4\sigma \right|, \tag{3}$$

their respective focal lengths (f_1, f_2) minimise, the difference between the resized spot $y_2 = \left(\frac{f_2}{f_1} \right) 4\sigma$ and the estimated core size $\bar{d}$. Figure 3(a) provides a diagram of the aforementioned acquisition process.
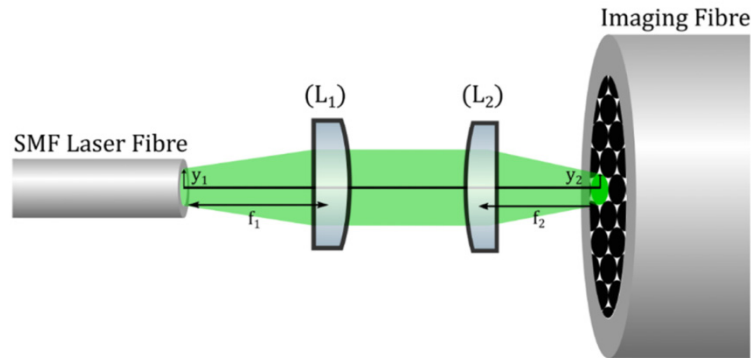
Fig. 2. Optical setup employing aspheric lenses L_1 and L_2, with corresponding of focal lengths of f_1 and f_2, to resize the Gaussian Point Spread Function (PSF) of an illuminating laser spot, preventing it from overlapping neighbouring cores.

Table 2. Fibre-coupled laser spots' Point Spread Functions (PSFs) measured at the end of the Single Mode Fibre (SMF) source at 520nm and 635nm. Mean nearest-neighbour spacing employed as estimate of core size.

	Size in pixels
Green: 520 nm (4σ)	13.9
Red: 635 nm (4σ)	14.8
Core size ($\bar{d}$)	15.9 (± 0.84)

(a)

(i)
Determine
SMF laser
PSF (y_1)

(ii)
Determine
core
separation (y_2)

(iii)
Estimate ratio
$$\frac{y_1}{y_2}$$

(iii)
Optimally select
aspheric lenses
L_1 and L_2
based on y_1/y_2

(b)

Repeat for total of 12 ROIs (300 cores)

(i)
Mount coherent fibre
bundle in x-y
translation stage
as in fig.1

(ii)
Uniformly illuminate
coherent fibre bundle
with same wavelength
as laser using widefield
image to focus fibre end

(iii)
Extract core size and
location parameters from
image

(iv)
Determine core-to-core
coupling statistics
for ROI

(v)
Use x-y translation
mount to illuminate
individual core within
coherent fibre bundle

(vi)
Acquire image of
core-to-core coupling

(vii)
Repeat image acquisition
for 5 randomly selected
cores within same ROI

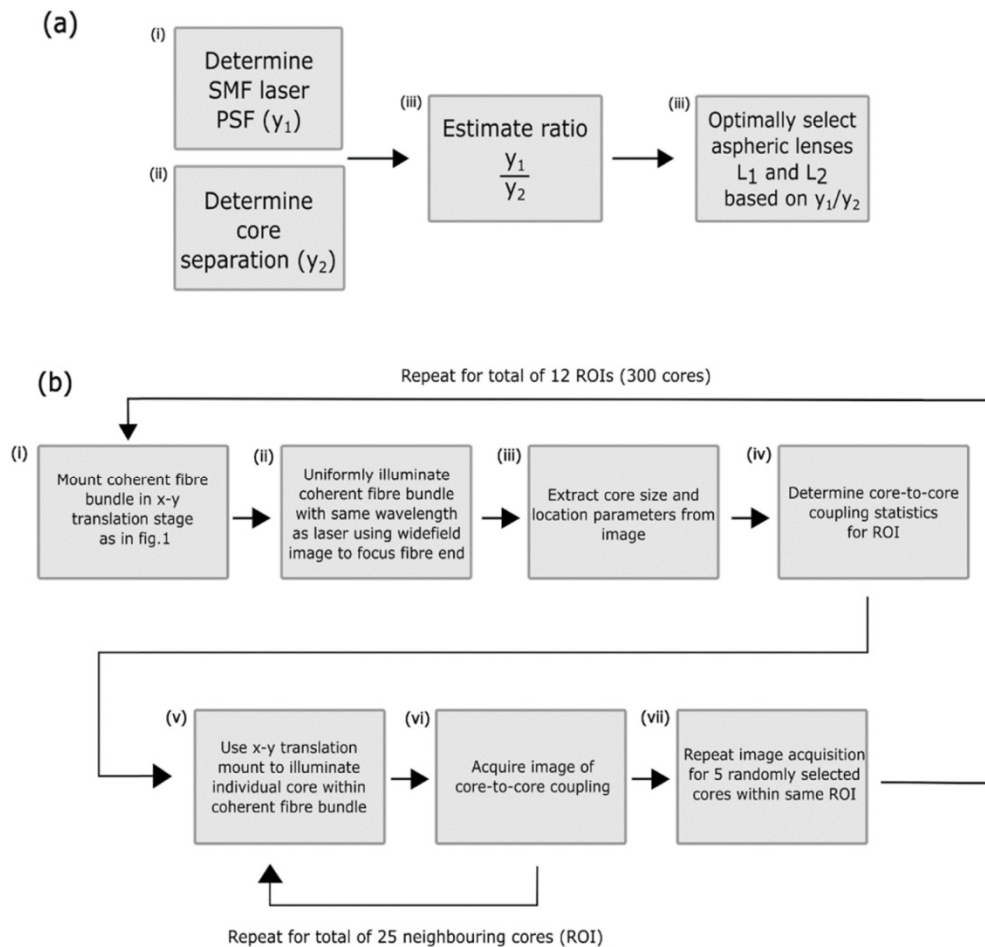Repeat for total of 25 neighbouring cores (ROI)

Fig. 3. Data acquisition protocols for (a) determining the focal lengths of aspheric lenses L_1 and L_2 to ensure optimal resizing of laser spots y_1 and y_2 so that light fills individual cores without overlapping to neighbouring cores, and (b) illuminating individual cores and capturing the coupled light across its immediate and extended neighbours.

2.2.2 Scanning multiple cores

Multiple regions-of-interest (ROIs) consisting of 25 neighbouring cores, each in a rectangular arrangement, were acquired for each wavelength. The power of the incident laser light along with the camera sensor properties were manually adjusted, at the start of the experiment, maximising the transmitted and recorded signal, without saturating the detector, while keeping noise in background (cladding) areas minimal. The position of the incident laser light was manually adjusted using the XY translational stage for every individual core. Optimal light positioning, illuminating the centre of the examined core, was visually assessed by two operators through imaging the camera end of the fibre, ensuring that preferential excitation of higher order modes was avoided. Prior to the acquisition of each 25-core ROI, a flood illumination image of the characterised fibre was captured. For 520 nm acquisition (green), a 470 nm (blue) LED source illuminated the camera end of the fibre. A fluorescein covered target was positioned to the laser end of the fibre. Uniform green fluorescence was transferred back through the fibre and imaged using the camera. Similarly, for 635nm acquisition (red), a 470 nm (blue) LED light source illuminated the distal end of the fibre. However, unlike the

green case, no target was placed at the laser end of the fibre. Instead, predominantly red fibre auto-fluorescence was imaged at the camera end. The flood illuminated images ensured that the imaging system was in focus at the camera end of the fibre for the each of the investigated acquisition wavelengths. Furthermore, they were employed to (i) segment the individual cores within the field-of-view (FOV) and (ii) extract all their associated size and location parameters relevant to the subsequent characterization. The LED illumination was not used for the subsequent fibre characterisation described. Following the acquisition of each 25-core ROI, 5 core locations were randomly selected and scanned again, in an attempt to assess the proposed acquisition setup's and methodology's robustness in terms of inter-core coupling repeatability. Figure 3(b) provides a diagram of the aforementioned acquisition process.

2.3 Analysis

The proposed analysis was performed individually on data from the two imaging wavelengths of interest, namely 520nm and 635nm. Figure 4 illustrates the basic steps of the data analysis.
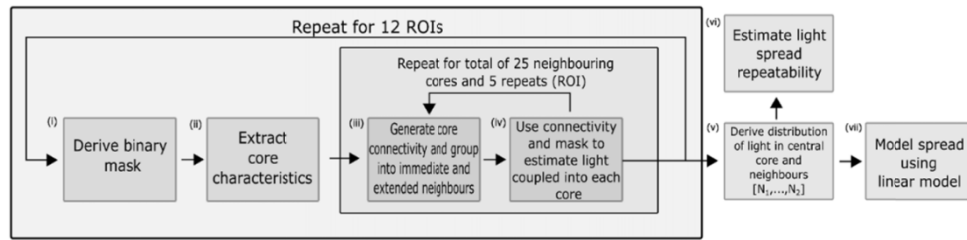

Fig. 4. Analysis protocol for measuring and quantifying coupling of light to the central (illuminated core) as well as its immediate and extended neighbours.

2.3.1 Extracting fibre core characteristics

Let $I_R(x, y)$ be a flood illumination greyscale image of a Region of Interest $(R = [1,12])$ of the coherent fibre bundle, with $x \in [1, N]$, $y \in [1, M]$ indicating the pixel location (x - column and y - row). For an image of L grey levels (8-bit, $[0, 1, 2, \ldots, L-1]$) the normalised histogram can be defined as a probability distribution

$$p_i = k_i / K, \text{ with } p_i > 0 \text{ and} \sum_{i=0}^{L-1} p_i = 1 \tag{4}$$

where, k_i and $K = M \times N = \sum_{i=0}^{L-1} k_i$ denoted the number of pixels with intensity level i, and the total number of pixels in the image respectively. Otsu's method was employed to recursively derive threshold $t \in [0, 1, \ldots, L-1]$, minimising the intra-class variance denoted by

$$\sigma_w^2(t) = q_1(t)\sigma_1^2(t) + q_2(t)\sigma_2^2(t) \tag{5}$$

with, weighting factors $q_1(t) = \sum_{i=0}^{t-1} p(i)$ and $q_2(t) = \sum_{i=t}^{L-1} p(i)$, class means

$\mu_1(t) = \sum_{i=0}^{t-1} ip(i)/q_1(t)$ and $\mu_2(t) = \sum_{i=t}^{L-1} ip(i)/q_2(t)$, and class variances

$\sigma_1(t) = \sum_{i=0}^{t-1} [i - \mu_1(t)]^2 p(i)/q_1(t)$ and $\sigma_2(t) = \sum_{i=t}^{L-1} [i - \mu_2(t)]^2 p(i)/q_2(t)$ By minimising the within class variance, Otsu's method maximises the separability (inter-class variance)

between the classes. Threshold t was employed to derive binary mask of the imaged fibre cores,

$$B_R(x,y) = \begin{cases} 1, & \{(x,y)|I(x,y) \geq t\} \\ 2, & \{(x,y)|I(x,y) < t\} \end{cases} \qquad (6)$$

with $x \in [1,N]$, $y \in [1,M]$. 8-connected components (i) smaller than 10 pixels (considered as artefacts at the imaged end of the fibre, such as dust, scratches, etc.), and (ii) connected to the image border (considered as not fully imaged cores), were removed from the binary mask $B_R(x,y)$.

Table 3. Properties extracted from the automatic analysis of the binary mask highlighting each core within a widefield microscopy (WFM) image of the fibre bundle.

Core Parameter	Notation	Description
Centroid	C_R	Centre of mass in X-Y coordinates.
Area	A_R	Actual number of pixels.
Major Axis Length	ML_R	Length of the major axis of an ellipse that best matches size & shape of core.
Minor Axis Length	mL_R	Length of the minor axis of an ellipse that best matches size & shape of core.
Orientation	O_R	Scalar specifying the angle between the *x*-axis and the major axis of the core.
Pixel List	PL_R	X-Y coordinates of the pixels that make up the core.

MatlabTM function regionprops was applied on binary mask $B_R(x,y)$ to (i) automatically identify cores centroids $C_R = [c_1, c_2, \ldots, c_P]$, where $c_i = (x_i, y_i)$ and P denotes the total number of cores imaged in I_R, and (ii) extract a range of shape parameters (Table 3) for each individual core in C_R. This information was utilised to estimate the percentage of core coverage across the imaged fibre $Q_R = \sum_{x=1}^{M} \sum_{y=1}^{N} B_R(x,y) / K$, as well as core size variability $W_R = \sigma_A / \mu_A$, where σ_A and μ_A corresponded to the mean and standard deviation within the core area vector $A_R = [a_1, a_2, \ldots, a_P]$. Furthermore, for core centroids $C_R = [c_1, c_2, \ldots, c_P]$, Delaunay Triangulation was employed to derive a connectivity list $DT(C_R)$ of the point set containing $(P-2)$ unique triangles. Delaunay Triangulation offers a number of attractive properties, including (i) connecting points in the nearest-neighbour manner, (ii) maximising the minimum angle of all the angles of the triangles (avoiding sliver triangles), and (iii) a circle circumscribing any triangle does not contain any other point in its interior. These properties, along with the quasi-hexagonal structure of the imaging fibre bundle make it an attractive approach for interpolating across the multicore fibre's honeycomb pattern [30]. For each core c_i, where i is the index of c_i in C_R, the associated rth -order neighbours of c_i in $DT(C_R)$, N_i^r for $r = [1,5]$, were estimated.

2.3.2 Quantifying cross coupling

Let $I_{c,R}(x,y)$ be a greyscale image of an individual core illumination and the associated cross coupling, with $x \in [1,N]$, $y \in [1,M]$ indicating the pixel location, and $c \in [1,25]$ since 25 cores were individually illuminated within a ROI $R = [1,12]$. Each, $I_{c,R}(x,y)$ was

automatically aligned to the corresponding flood illuminated image of the fibre $I_R(x,y)$. For the alignment, the optimal image translation $T(x,y)=(x+t_x,\ y+t_y)$, with $t_y \in [1,N]$ and $t_y \in [1,N]$ being the shift along the x and y coordinates of the image, was estimated by maximising (through Gradient Descent) the similarity S (Normalised Cross Correlation) between the two images

$$\arg\max_{t_x t_y} S(I_R, T(I_{c,R})).\tag{7}$$

For each aligned image $I'_{c,R}$ within a 25-core ROI, the mean intensity $J^0_{c,R}$ across the active region $(PL_R(i))$ in binary mask B_R associated with the central core (c_i) was estimated, where i corresponded to the index of core c_i in C. Similarly, the mean intensities $J^r_{c,R}$ at each of the r th-order neighbouring cores in $\left[N^1_i, N^2_i, \ldots, N^5_i \right]$ was estimated for $r=[1,5]$. For each of the 25-core ROIs $(R=[1,12])$, a vector holding the intensity for each of the cores in the centre $\left(J^0_{T,R}=[J^0_{1,R},\ldots,J^0_{25,R}]\right)$, as well as a matrix holding the core intensities within each layer of the r th-order neighbours $\left(J^r_{T,R}=[J^r_{1,R},\ldots,J^r_{25,R}], r=[1,5]\right)$ were defined. Furthermore, in a similar approach, matrices holding the mean intensity for each of the cores in the centre $\left(J^0_{TT}=[J^0_{T,1},\ldots,J^0_{T,12}]\right)$, and each of the cores within a layer of immediate and extended neighbours $\left(J^r_{TT}=[J^r_{T,1},\ldots,J^r_{T,12}], r=[1,5]\right)$, for all 12 ROIs, were defined.

2.3.3 Assessing the robustness of the acquisition method

A number of factors quantify the robustness of the proposed methodology (i) measuring the stability of the laser source, (ii) ensuring optimal focal planes at both the illumination and imaging ends of the coherent fibre bundle, and (iii) determining the repeatability of the cross coupling measurements. To assess the first two factors, the mean and standard deviation (over the 25 cores scanned) of the overall light as well as of the proportion of the light coupled in the central cores $\left(\mu^0_R, \sigma^0_R\right)$ and each of $r=[1,5]$ neighbouring core layers $\left(\mu^0_R, \sigma^0_R\right)$ was estimated over multiple ROIs $(R=[1,12])$. For no drift in laser power as well as the focal planes in both fibre ends, there should be no systematic variation in the measured power range over the 12 different ROIs.

To assess the repeatability of cross coupling, the measurement of 5 cores within each 25-core ROI were randomly repeated. For each of the repeated cores $cr \in [1,5]$, vectors $JJ^r_{cr,R}$ for $r=[0,5]$ containing the intensity at the central core and each layer of neighbours were derived as described in the Quantifying cross coupling section. A profile of the cross coupling spread for each of the 25 original and 5 repeated measurements was defined as $\left[J^0_{c,R}, J^1_{c,R}, \ldots, J^5_{c,R}\right]$ and $SP'_{cr,R}=\left[JJ^0_{cr,R}, JJ^1_{cr,R}, \ldots, JJ^5_{cr,R}\right]$ respectively. The repeatability of the cross coupling profile between the repeated measurements and each of the original measurements was estimated using Normalised Mutual Information (NMI) [31]

$$Y(SP_c, SP'_{cr}) = \frac{H(SP_c)+H(SP'_{cr})}{H(SP_c, SP'_{cr})}\tag{8}$$

for $c \in [1,25]$ and $cr \in [1,5]$. $H(U)$, $H(V)$ and $H(U,V)$ described the marginal and joint entropies [31], as a measure of information, within the vectors SP_c and SP'_{cr}. Figure 5 provides a diagram of the aforementioned process.

2.4 Modelling inter-core coupling and its effect on simulated images

The information derived through the analysis described above and summarised by distributions $J^{cntr}_{total\,R}$ and $J^{r}_{total\,R}$ was used to create a forward linear model of the average light cross coupling across a coherent fibre bundle. More precisely, $u \in \mathbb{R}^{N_1}$ was defined as a column vector containing the total fluorescent light of the original scene at the locations of each core of a coherent fibre bundle. The observed (vectorised) OEM image $v \in \mathbb{R}^{N_1}$, as imaged through a coherent fibre bundle, was then modelled by linear model

$$v = Hu + w \tag{9}$$

where, $H \in \mathbb{R}^{N_1 \times N_1}$ was the matrix representation of a convolutional operator modelling cross coupling between fibre cores. Vector $w \in \mathbb{R}^{N_1}$ represents the additive observation noise and model mismatch and was assumed to be a white Gaussian noise sequence. The kth row in H contained the weighted contributions of each individual core in the fibre bundle relative to the total light coupled into the k th core. In particular, weighted contributions $\left[W^0, W^1, W^2, \ldots, W^5 \right] \in \mathbb{R}[0,1]$ indicated the proportion of light in the k th core originating from the k th core (W^0) itself, its immediate (W^1) or its extended neighbours ($W^2, \ldots, W^5$). The weighted contributions were derived through distributions $J^0_{T,R}$ and $J^R_{T,R}$ ($r \in [1,5]$) respectively. The remaining entries of matrix H that do not correspond to an immediate or an extended neighbour were set to 0.
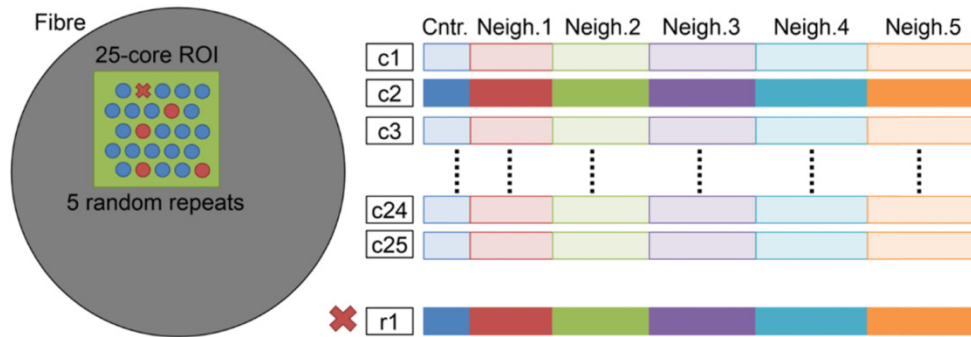

Fig. 5. Diagram describing the process of repeating 5 cores within a 25-core region of interest (ROI), vectorising the coupling pattern extracted from the associated images [c1,…, c25], and identifying the matching original core based on the coupling pattern similarity. In this example, the vectorised pattern of repeated core r1 matches with c2, the second core in the 25-core ROI.

3. Results

3.1 Fibre core characteristics

For each of the 12 ROIs in each acquisition wavelength (520 nm and 635nm) a corresponding widefield microscopy (WFM) image of the coherent fibre bundle was acquired. Similarly, a Scanning Electron Microscopy (SEM) image of the coherent fibre bundle characterised was also acquired and analysed. Figure 6 illustrates a visual comparison between the SEM and an example WFM image of the fibre imaging a uniform fluorescent target (470 nm excitation,

520 nm emission). Figure 6 also provides an example of the binary image, derived using Otsu's method, highlighting the pixels corresponding to fibre cores. The binary representations of the imaged fibre were used for the subsequent analysis deriving (i) fibre and core characteristics, (ii) core relations, and at a later stage (iii) light spread amongst neighbouring cores. Table 4, summarises the fill ratio and core size variability characteristics of the fibre, estimated using the 3 imaging modes mentioned, (SEM, WFM-635nm and WFM-520nm). For the WFM data, since multiple (12) ROIs were acquired for each wavelength, the mean and standard deviation is provided. Figure 7 provides examples of the Delaunay core triangulation $DT(c_i)$ and consequent neighbouring core interdependences, from the central, illuminated core (c_i), to its immediate and extended neighbouring layers $\left(N_i^1, N_i^2, N_i^3, N_i^4, N_i^5\right)$.

3.2 Cross coupling quantification

For each of the scanned cores, the locations of the immediate and extended neighbours along with the corresponding binary masks, as illustrated in Fig. 7, were employed to quantify the extent of light cross coupling. Figure 8 provides characteristic examples, 3 for each acquisition wavelength, of light coupling spreads from the central to the neighbouring cores. The coupling spread patterns were broadly categorised into three classes, (i) relative even spread amongst neighbours, fading with distance, (ii) seemingly random spread in both location and magnitude across the neighbourhood, and (iii) a combination of the even spread implanted with random cores of high coupling. For every scanned core, the proportion of overall light remaining in the central core $J_{TT}^0 / \sum_{r \in [0,...,5]} J_{TT}^r$ as well as the proportion of light coupled in each rth order neighbouring cores $J_{TT}^r / \sum_{r \in [0,...,5]} J_{TT}^r$ for $r = [1,...,5]$ was estimated. Figure 9 and Fig. 10 visualise the distribution of light proportion coupled in the central cores as well as the cores of each neighbouring layer, for each acquisition wavelength (520 nm and 635nm). Table 5 quantifies the location and spread of above distributions through the mean, median and standard deviation of the proportion of light coupled in the central and each neighbouring core (grouped in relevant layers). Similarly, Table 6 provides the mean and median proportion of light coupled in the central core and each layer of immediate and extended neighbours as a whole. Finally, Fig. 11 illustrates the relationship of the proportion light coupled to a core, and its distance (in pixels) to the central (illuminated) core for both acquisition wavelengths. The cores are grouped to the relevant 5 neighbouring layers.
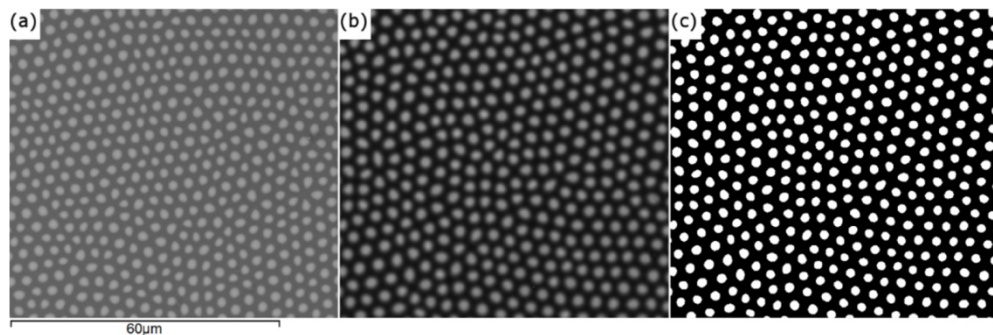

Fig. 6. Characteristic examples of (a) Scanning Electron Microscopy (SEM), and (b) widefield microscopy (WFM – 635nm) of a coherent fibre bundle. (c) An example of the binary image, derived using Otsu's method on a WFM image, highlighting the pixels corresponding to fibre cores.

Table 4. Fibre properties as extracted from different imaging modes.

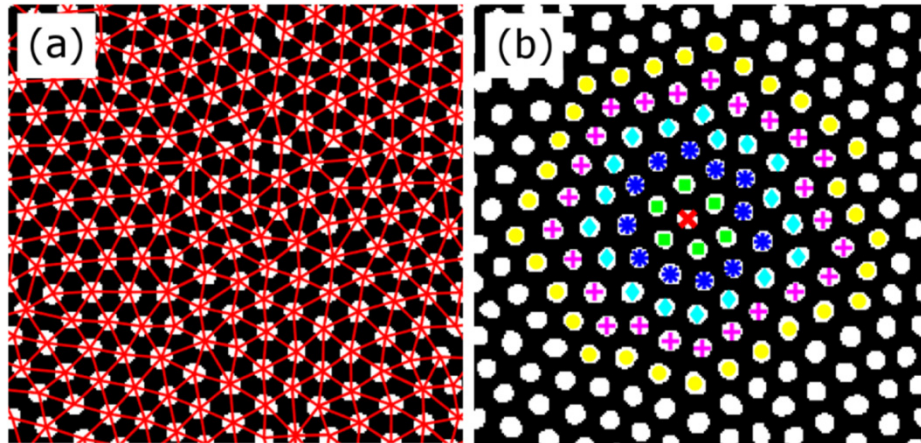|	SEM	WFM 520nm	WFM 635nm
Fill Ratio (%)	31.0	32.3 (± 1.5)	29.5 (± 0.3)
Core size variability (%) $(\sigma(Area)/\mu(Area))$	14.1	16.9 (± 1.1)	9.4 (± 0.6)

Fig. 7. Example of a binary mask highlighting the cores with (a) the relevant Delaunay triangulation linking cores, and (b) the associated grouping of cores to immediate (green) and extended neighbours (blue, cyan, magenta and yellow).
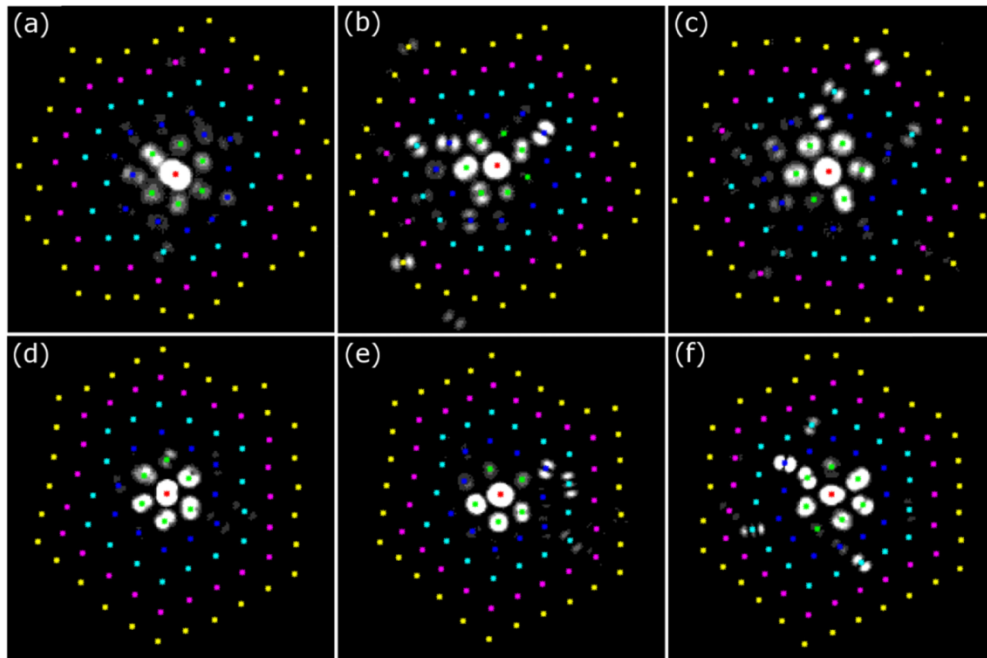

Fig. 8. Examples of coupling spread patterns broadly categorised into three classes with, (a) and (d) relative even spread amongst neighbours, fading with distance, (b) and (e) seemingly random spread in both location and magnitude across the neighbourhood, and (c) and (f) a combination of the even spread implanted with random cores of high coupling. Examples for both acquisition wavelengths provided – 635nm (top) and 520nm (bottom).
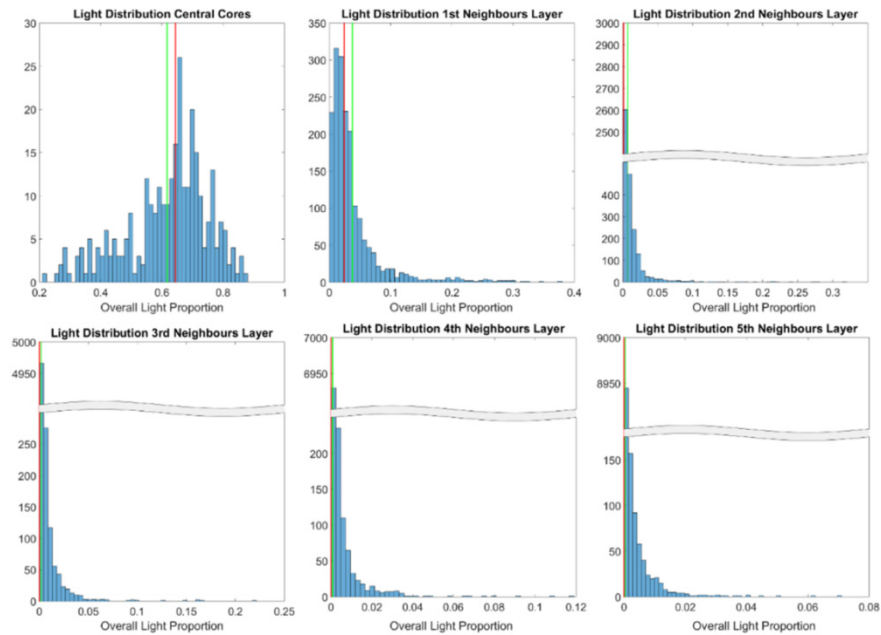
Fig. 9. Histograms providing a visual representation of the distributions of the proportion of light at 635nm coupled in the central core as well as the cores of each of the neighbouring layers. The mean and median (green and red lines respectively) proportion of light for the cores of each layer are also provided.
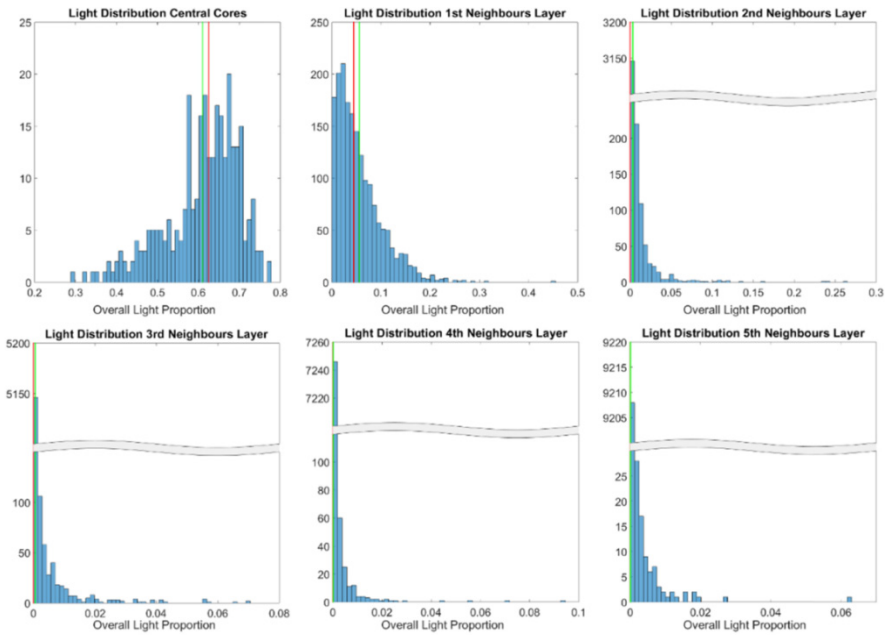

Fig. 10. Histograms providing a visual representation of the distributions of the proportion of light at 520nm coupled in the central core as well as the cores of each of the neighbouring layers. The mean and median (green and red lines respectively) proportion of light for the cores of each layer are also provided.
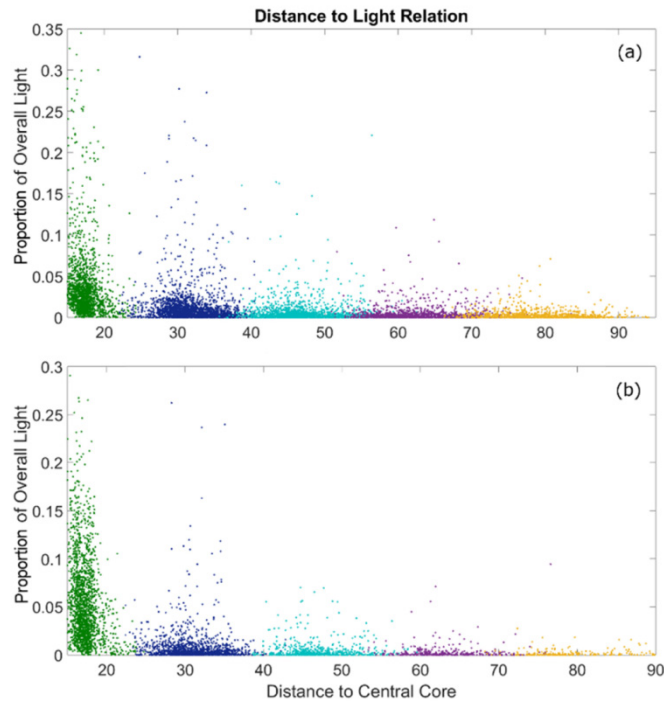
Fig. 11. Plots of the distance (in pixels) of each core to the corresponding central (illuminated) core against the associated proportion of light coupled through the core at (a) 635nm and (b) 520nm. Cores are grouped into their respective neighbouring layers from immediate (green) to extended (blue, cyan, magenta and yellow).

Table 5. Coupling per individual core. Mean, standard deviation and median of the proportion of light coupled in the central and each neighbouring core (grouped in relevant layers).

	520nm		635nm	
	Mean (SD)	**Median**	**Mean (SD)**	**Median**
Cntr.	61.0 (9.1)	62.5	61.7 (13.6)	64.5
1st	5.6 (4.7)	4.4	3.8 (4.5)	2.4
2nd	3.1 (1.2)	0	0.7 (1.9)	0.1
3rd	0.1 (0.4)	0	0.2 (0.8)	0
4th	0.0 (0.2)	0	0.1 (0.4)	0
5th	0.0 (0.1)	0	0.0 (0.2)	0

Table 6. Coupling per neighbouring layer. Mean and median of the proportion of light coupled in the central core and each layer of immediate and extended neighbours as a whole.

	520nm		635nm	
	Mean	**Median**	**Mean**	**Median**
Cntr.	61.0	62.5	61.7	64.5
1st	33.6	26.5	22.7	14.6
2nd	3.8	0	8.9	1.6
3rd	1.1	0	3.6	0
4th	0.4	0	2.0	0
5th	0.2	0	1.1	0
Total	100.0	89.0	100.0	80.7

3.3 Robustness of acquisition method

To assess if there was a substantial and/or systematic drift in the laser power for the duration of the experiment, or if there was a focal drift in either the imaging or illumination end of the

fibre, the light coupled through (i) the whole fibre, (ii) the central core, and (iii) each of the immediate and extended neighbouring core layers was measured and analysed. Figure 12(a) plots the mean and standard deviation (over the 25 cores within each ROI) of the total light coupled through the fibre over the duration of the acquisition process (12 ROIs). Similarly, Figs. 12(b) and 12(c) plot the mean and standard deviation (over 25 cores) of the proportion of the light coupled through the central cores $\left(\mu_R^0, \sigma_R^0\right)$ and each of $r = [1,5]$ neighbouring core layers $\left(\mu_R^0, \sigma_R^0\right)$ over $R = [1,12]$ ROIs.

Figure 13 provides some examples to illustrate how repeatable the measured coupling patterns were throughout the proposed data acquisition process. More precisely, in each line graph, the similarity of the coupling pattern of a repeated core was measured against the coupling patterns of all the 25 cores in the associated ROI. For the 635nm acquisition wavelength, only 1 of the 60 repeated cores (1.7%) did not demonstrate maximum similarity with the matching original core. On the other hand, for the 520nm wavelength, 42 of the 60 repeated cores (70%) demonstrated a single peak with global maximum similarity with the matching original cores. A further 11 repeated cores (18%) demonstrated multiple peaks of high similarity within the 25-core ROI, with the matching original core yielding a local maximum in similarity very close in value to the associated global maximum value. The remaining cores (12%) demonstrated low levels of repeatability (potentially not peaking). The histograms in Fig. 14 illustrates the distribution spread of the coupling pattern similarity between the repeated cores and their matching original cores (blue), as well as the similarity between the repeated cores and the other 24 cores in their respective ROI (orange).

3.4 Cross coupling effect and computational rectification

To assess the effect of the estimated light coupling across neighbouring cores, simulated data, as imaged through a coherent fibre bundle, of the USAF 1951 chart were generated. In particular, the distal end of the imaging fibre was positioned in contact with a standard chrome on glass USAF 1951 target (Thorlabs, R1DS1N). This measurement was done by allowing the fluorescence from a target (fluorescent block, Chroma) in the spectral range of 510 to 560 nm to pass through the test target, transmitted through the imaging fibre and being imaged back through the optical system in the conventional manner for widefield endomicroscopy [11, 12]. Figure 15(a) illustrates a binary image of the chart, commonly used in the assessment of optical systems. A core location pattern from a real OEM data with the same dimensions as the chart in Fig. 15(a) was employed to simulate the effect of the irregular sampling process dictated by the nature of the imaging fibre bundle. Figure 15(b) illustrates the resulting image, sampling the chart at the core locations and interpolating between the irregular samples to generate a continuous image of the same size. Figure 15(c) applies the light inter-core coupling spread, as measured and summarised in Table 6 (median at 520nm), at the simulated USAF chart image in Fig. 15(b). Figure 16 plots the cross-sections before and after cross coupling is applied to the simulated images at two different locations to illustrate the effect of cross coupling in features of different sizes. Finally, some real OEM images of the USAF chart are provided in Fig. 15, (d) prior to any sampling/interpolation, (e) after linear interpolation removing the core honeycomb patterns, and (f) after cross coupling has been computationally removed from the real data. An optimisation based, deconvolution and restoration method utilising the Alternating Direction Method of Multipliers algorithm, as described by Karam et al. [32], was employed.
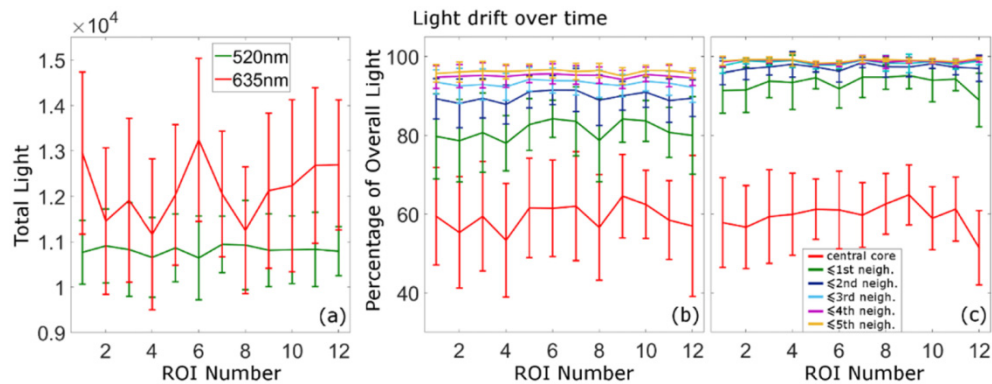
Fig. 12. Overall light variation over the duration of the acquisition process (12 ROIs) (a) transmitted along the whole fibre, and (b-c) as a proportion coupled through the central core and cumulatively each neighbouring layer at 635nm and 520nm respectively.
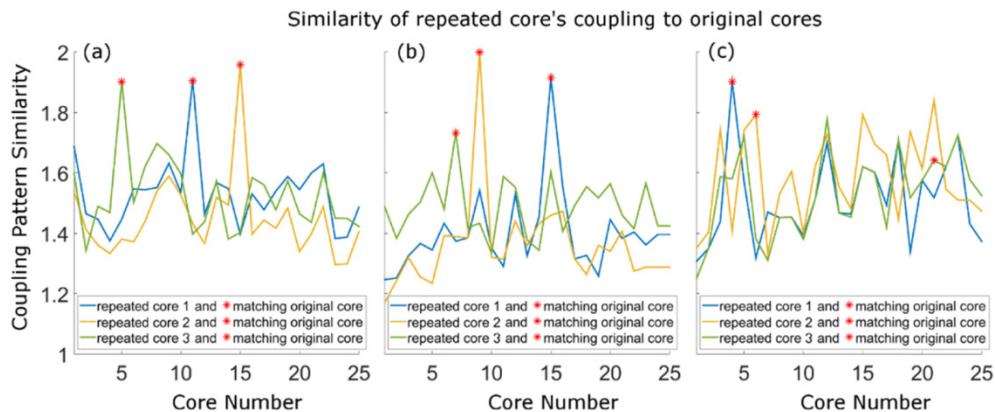

Fig. 13. Illustrative examples of coupling pattern similarity (NMI) of a repeated core against the coupling patterns of all the 25 cores in the associated ROI. In particular, each line illustrates the measured similarity (NMI) between the coupling pattern of a chosen repeated core against the coupling patterns of all the 25 cores in the associated ROI. The asterisk indicates the number of the core within the 25-core ROI that matches the chosen repeated core. High similarity is expected for matching cores (asterisk). (a) Three repeated core examples within a 25 core ROI using 635nm acquisition wavelength, (b-c) six further examples, from two different ROIs, using 520nm acquisition wavelength.

4. Discussion

Figure 6 and the quantitative fibre characteristics in Table 4 indicate that the WFM images of the fibre bundle and the corresponding binary masks, utilised throughout the coupling analysis in this study, provide a good match to the SEM image of the same fibre. The fill ratio estimate appears to be largely unaffected by the imaging mode. The minor effect of the imaging mode on the estimated core size variability is to be expected, with SEM mapping the actual size and shape of each core's doped region (through electron scattering properties) while the WFM data images the shape of the combined fundamental and higher order modes transmitted through each core. Lower wavelengths (520nm) can excite more optical modes in a single core, potentially generating a more complex illumination pattern for each core, hence increasing the estimated core size variability when compared to the higher wavelength acquisition (635nm). Nonetheless, the core size variability in all three imaging modes is of the same order of magnitude (fluctuating around the SEM estimate) and is expected to be of no relevance in the subsequent cross coupling analysis.
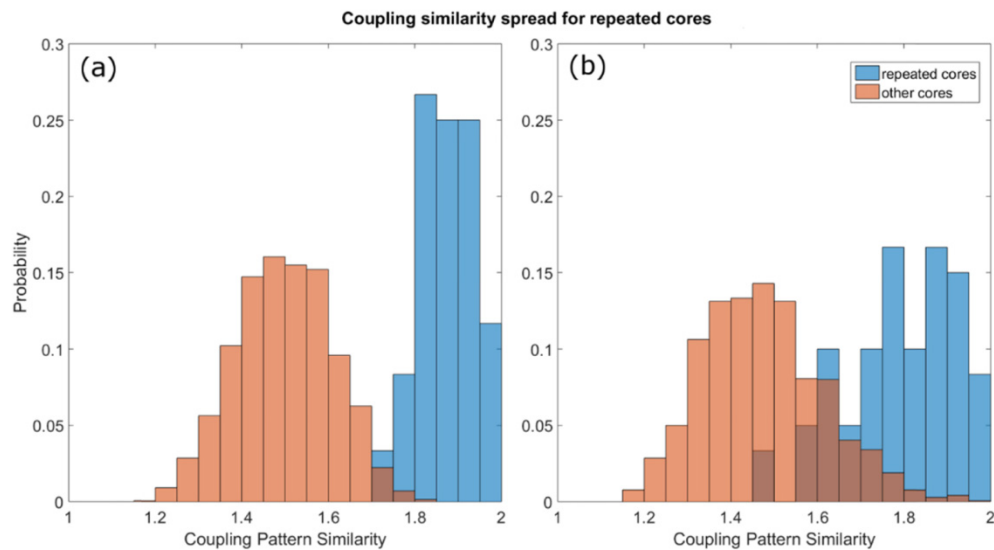
Fig. 14. Distribution spread of the coupling pattern similarity between the repeated cores and their matching original cores (blue), as well as the similarity between the repeated cores and the other 24 cores in their respective ROI (orange), at (a) 635nm and (b) 520nm.
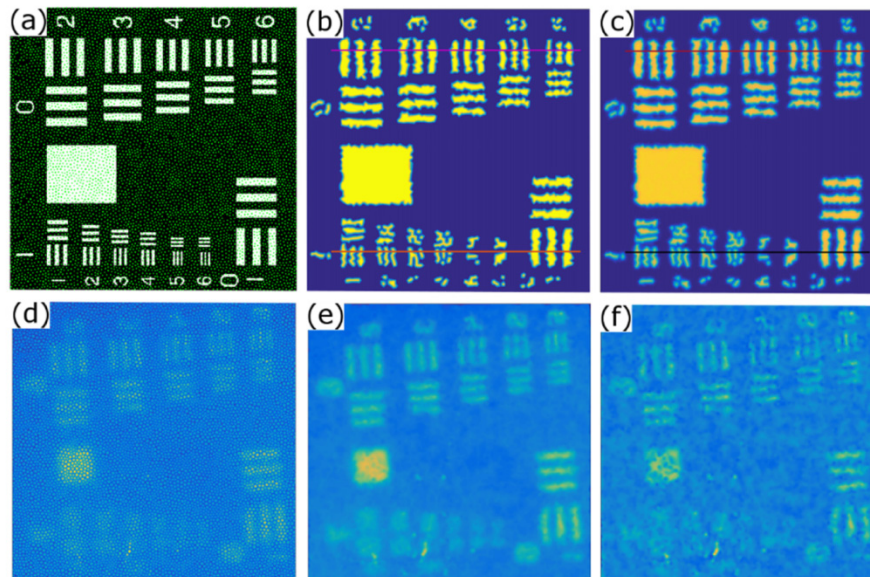

Fig. 15. Example of cross coupling effect on simulated (a-c) and real (d-f) OEM images of the USAF chart. (a) Binary image of USAF chart, fibre-core locations overlaid, (b) interpolated image of USAF chart, based on values at core locations, (c) interpolated image after applying estimated cross coupling. (d) Real OEM image of fluorescent USAF chart. (e) Interpolated version of (d), based on values at core locations. (f) post processed version of (e), estimating the original de-convolved data.

4.1 Cross coupling quantification

As highlighted in the examples of Fig. 8, the light coupling spread patterns can be broadly categorised into three classes, demonstrating (i) a relatively even spread amongst neighbours, fading with distance from the central core, (ii) a seemingly random spread in both location and magnitude across the neighbourhood, and (iii) a combination of the even spread

implanted with random cores of high coupling. While the extent of the coupling spread varies, these three broad coupling classes occur at both acquisition wavelengths (520mm and 635nm). Furthermore, the coupling pattern for an individual core can be affected by the curvature, and thus the movement, of the coherent fibre bundle. Consequently, quantifying the overall spread of light to neighbouring cores for each wavelength, instead of individual coupling patterns, provides a more robust statistical characterisation largely unaffected by individual coupling patterns and therefore resistant to fibre bending. In particular, in both cases the percentage of light coupled along the central core is measured to be very similar (mean: 61.0% for 520nm vs 61.7% for 635nm, median: 62.5% for 520nm vs 64.5% for 635nm). However, as expected from their respective wavelengths, the overall coupling spread of the 635nm tends to be wider in comparison to the spread at 520nm. This can be observed Fig. 8 as well as in the quantitative core coupling information summarised in Tables 5 and 6. As illustrated in Fig. 11, while overall coupling tends to decrease with distance from the central core, when observed in terms of individual neighbouring layers there appears to be no direct correlation between small distance changes and relevant light coupling changes. Consequently, the subsequent analysis was based on grouping cores into neighbouring layers rather than explicitly estimating and considering the distance of a core to the relevant illuminated central core.

Figures 9 and 10, provide a visual representation of the proportion of light-coupling distributions recorded at each of the central cores as well as the corresponding immediate and extended neighbours. The main body of each distribution tends to correspond to the relatively even light cross coupling [Figs. 8(a) and 8(d)]. The tails of each distribution tend to correspond to the small number of occurrences with high coupling that are seemingly randomly distributed across the neighbourhood [Figs. 8(b) and 8(e))]. Such outlying measurements, while not very common can affect the estimated mean value for each neighbouring layer. This is obvious by the substantial drop between the estimated mean and (more robust) median values for each of the neighbouring layers (Tables 5 and 6). The heavier tails in the distributions for 635nm (when compared to 520nm) indicate that this wavelength is affected to a greater extent from random cores that demonstrate high levels of coupling with the central core. This larger effect at 635nm is also apparent in the estimated median percentages of light-coupling for each neighbouring layer, accounting for 80% and 89% of the overall light at 635nm and 520nm respectively. The seemingly random cores exhibiting large coupling can be attributed to random matches across a range of physical properties (including core size and shape) between neighbouring core pairs. The larger light spread at 635nm increases the chances for light to reach a core with closely matching properties, hence generating a disproportionate and apparently random coupling. Since this behaviour is very difficult to predict in practice, the median value for each neighbouring layer is perceived to be a more representative measure of the even light coupling spread, as required for the proposed linear model for fibre cross coupling.

4.2 Robustness of acquisition method

The stability of the acquisition setup and the robustness of the acquired data is of paramount importance in the derivation of the information required to generate a linear model representative of the underlying cross coupling. Figure 12 illustrates that (for both wavelengths) there is no substantial or systematic fluctuation in the mean light transmitted along the whole fibre [Fig. 12(a))] as well as along each of the individual neighbouring layers. Smaller non-systematic variations, expressed in the form of variability within each ROI (standard deviation) and across the different ROIs (mean), can be associated with the particular properties of each illuminated core. The relatively larger variability in overall light transmission along the fibre at 635nm can be attributed to (i) variable input coupling, with longer wavelengths coupling to less optical modes and hence fewer opportunities to couple efficiently, and (ii) possible more lossy transmission at longer wavelengths, though this is

something that needs to be investigated further. Nevertheless, this coupling variability is not substantial, nor systematic, suggesting a stable illumination laser power and no drift in the focal planes (at either end of the fibre) throughout the acquisition process.
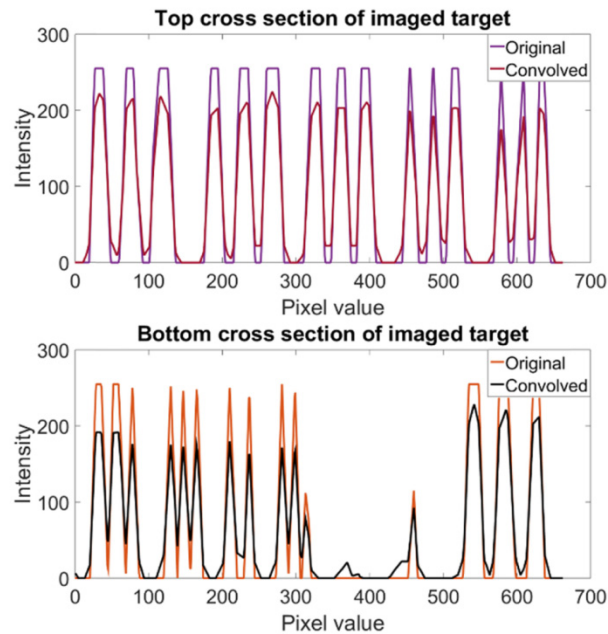

Fig. 16. Cross sections across the top, and bottom of the original and the cross-coupled simulated images in Fig. 15 (b) and (c).

Another important property of the proposed fibre characterisation and modelling approach is the repeatability of the coupling patterns for a given core at a given wavelength. In order to quantitatively assess such coupling pattern repeatability, repeated measurements were performed for 5 cores within each 25-core ROI (60 repeated cores at each wavelength). Figure 13 provides some representative examples of the similarity of the repeated core's coupling pattern when compared with the coupling patterns of each of the 25 cores in the ROI. In most cases, the core that was repeated (asterisk on each line graph of Fig. 13) demonstrates a sizeable global maximum peak relative to the similarity of the remaining cores of the ROI [Figs. 13(a) and 13(b)]. This is also illustrated in the histograms of Fig. 14, with the repeated cores demonstrating on average higher similarities relative to the remaining cores of the ROI. Some of the observed drop in similarity amongst repeated cores can be attributed to changes in the coupling patterns due to small fibre movements throughout the experiment. Furthermore, there are cases with numerous high peaks amongst the 25 cores in the ROI [Core 2 in Fig. 13(c)]. Such behaviour is observed in cores with uniform coupling spread, a pattern that is common within a 25-core ROI. Such multiple peaks are more likely to occur at 520nm since the coupling spread is narrower and less affected by random highly-coupled cores than 635nm (Table 6). Hence the longer tail in the similarity distribution of the non-repeated cores (Fig. 14). Nevertheless, the repeated core tends to correspond to one, if not the largest, of the local maxima in the relevant similarity curve. Finally, there are cases, such as the example in Core 3 in Fig. 13(c), in which the coupling pattern is not as repeatable as anticipated. This behaviour is observed more often at the shorter wavelengths (520nm) where a larger number of modes can be excited. Small misalignments during the repeated core acquisition can therefore result in variable mode excitation and consequently to a different, usually more irregular coupling pattern. Hence the wider spread (towards the lower end) of the pattern similarity distribution at 520nm. However, the proposed approach cannot (and

does not attempt to) model such irregular and seemingly random coupling patterns. Instead the overall coupling spread is modelled. Hence, any pattern similarity drop due to light misalignment and fibre motion should not affect the estimated overall coupling statistics. Consequently, the repeated cores of interest exhibit consistently high repeatability in both wavelengths, with 98.3% of repeated cores achieving global maximum peak similarity with the matching original cores at 635nm, and 88% of repeated cores achieving high similarity [a global or high local maximum as in Cores 1 and 2 in Fig. 13(c) respectively] with the matching original core at 520nm.

4.3 Cross coupling effect and computational rectification

Past studies have employed coupled mode theory to redesign fibres in order to minimise coupling. However, due to physical limitations dictating a trade-off between core-spacing (image resolution) and coupling, these approaches are yet to completely remove the coupling effect in coherent fibre bundles, which to date remains a major limitation in OEM. The strength of the proposed analysis is that it enables the derivation of a simple linear model $(v = Hu + w)$ to describe the overall light spread across neighbouring cores. This model does not try to incorporate information relating to the individual coupling patterns, that can vary considerably across different cores and be affected by fibre curvature. Instead, a robust measurement (median) is derived from the associated distributions, providing a representative value for the light coupled in the central core and each of the neighbouring cores. As illustrated by the simulated data in Fig. 15 and Fig. 16, the proposed model provides a close match to the substantial image degradation observed in real OEM data. Such light spread amongst neighbouring cores makes the detection (both visually as well as through automated image analysis approaches) of small structures (such as stained bacteria) over bright background (such as lung tissue) a challenging task [12]. Any additional degradation observed in the real OEM data can be attributed to a number of factors, such as (i) the limited optical resolution of the acquisition system, and (ii) the non-uniform LED illumination of the field of view, all of which are beyond the scope of this study. By feeding the measured coupling extent to a simple linear model $(v = Hu + w)$ the original de-coupled data can be estimated [Fig. 15(f)]. The problem of estimating u (original intensities at cores) from v (observed, cross-coupled data) is a linear inverse problem (LIP), akin to image restoration and reconstruction approaches used in a range of applications [26, 27, 33]. For most scenarios of practical interest, this is an ill-posed LIP (IPLIP), i.e. matrix H is singular and/or very ill-conditioned. Most state-of-the-art methods for dealing with such linear inverse problems consider the unconstrained problem

$$\min_x \frac{1}{2}\left\| Hu - v \right\|_2^2 + \lambda \phi(u) \tag{10}$$

with $\left\| . \right\|_2$ being the common ℓ_2-norm, and $\phi \colon \mathbb{R}^N \leftarrow \overline{\mathbb{R}} = \mathbb{R} \bigcup \{-\infty, +\infty\}$ being the regularisation function whose influence is controlled by the regularisation parameter $\lambda \in \mathbb{R}_+$. A plethora of state-of-the art approaches can be employed to solve the deconvolution and restoration problem as formulated in (10). These approaches can be broadly categorised into optimisation-based and simulation-based approaches. Karam et al. [32] have demonstrated the potential of such approaches in reconstructing OEM data. Modelling and computationally compensating (deconvolving) for inter-core coupling across coherent fibre bundles can therefore provide a potential solution in its own right, or act as a powerful adjunct to data acquired with novel, optimised fibres.

4.4 Future work

While beyond the scope of this study, there are numerous opportunities to employ the proposed fibre assessment. In particular, repeated inter-core coupling characterisation, as proposed in this study, can be performed in a number of identical fibres (same build properties). This analysis can specify whether a single cross coupling spread distribution suffices for characterising a specific type of fibre or if individual fibre characterisation is necessary. Furthermore, characterisation and comparison of alternative coherent imaging fibres [23, 28], at several additional operational wavelengths, such as in the infra-red region, is also of interest. Finally, the development and assessment of algorithms that employ the measured cross coupling spread and can computationally compensate, ideally in real-time, for the associated image degradation, is highly desirable.

5. Conclusions

Inter-core coupling is a well-recognised limitation in coherent fibre bundles, potentially masking out fine details in clinical OEM images. This study proposed a novel approach for measuring and quantifying inter-core coupling, in terms of overall spread on immediate and extended neighbouring cores. Robust distribution estimation of cross coupling spread at 520nm and 635nm demonstrated the feasibility of the proposed approach. The quantified cross coupling spread can be fed into a simple linear model, which in turn can be employed to computationally estimate (inverse problem) the underlying, de-coupled data. Future directions include (i) the inter-core coupling characterisation across a range of coherent fibre bundles used in OEM, and (ii) the development of novel and efficient algorithms that can computationally compensate for inter-core coupling and the associated image degradation.